
LEARNING-AUGMENTED PERFORMANCE MODEL FOR TENSOR PRODUCT FACTORIZATION IN HIGH-ORDER FEM

A PREPRINT

Xuanzhengbo Ren
 Graduate School of Informatics
 Nagoya University
 Nagoya, Japan
 ren@hpc.itc.nagoya-u.ac.jp

Yuta Kawai
 RIKEN R-CCS
 Kobe, Japan

Tetsuya Hoshino
 Information Technology Center
 Nagoya University
 Nagoya, Japan

Hirofumi Tomita
 RIKEN R-CCS
 Kobe, Japan

Takahiro Katagiri
 Information Technology Center
 Nagoya University
 Nagoya, Japan

Daichi Mukunoki
 Information Technology Center
 Nagoya University
 Nagoya, Japan

Seiya Nishizawa
 RIKEN R-CCS
 Kobe, Japan
 *

January 13, 2026

ABSTRACT

Accurate performance prediction is essential for optimizing scientific applications on modern high-performance computing (HPC) architectures. Widely used performance models primarily focus on cache and memory bandwidth, which is suitable for many memory-bound workloads. However, it is unsuitable for highly arithmetic intensive cases such as the sum-factorization with tensor n -mode product kernels, which are an optimization technique for high-order finite element methods (FEM). On processors with relatively high single instruction multiple data (SIMD) instruction latency, such as the Fujitsu A64FX, the performance of these kernels is strongly influenced by loop-body splitting strategies. Memory-bandwidth-oriented models are therefore not appropriate for evaluating these splitting configurations, and a model that directly reflects instruction-level efficiency is required. To address this need, we develop a dependency-chain-based analytical formulation that links loop-splitting configurations to instruction dependencies in the tensor n -mode product kernel. We further use XGBoost to estimate key parameters in the analytical model that are difficult to model explicitly. Evaluations show that the learning-augmented model outperforms the widely used standard Roofline and Execution-Cache-Memory (ECM) models. On the Fujitsu A64FX processor, the learning-augmented model achieves mean absolute percentage errors (MAPE) between 1% and 24% for polynomial orders (P) from 1 to 15. In comparison, the standard Roofline and ECM models yield errors of 42%–256% and 5%–117%, respectively. On the Intel Xeon Gold 6230 processor, the learning-augmented model achieves MAPE values from 1% to 13% for $P = 1$ to $P = 14$, and 24% at $P = 15$. In contrast, the standard Roofline and ECM models produce errors of 1%–73% and 8%–112% for $P = 1$ to $P = 15$, respectively.

Keywords High-Order FEM, Tensor Product Factorization, Performance Modeling, Instruction-Level Parallelism, Learning-Augmented Modeling

1 Introduction

Performance modeling is an effective technique for gaining insights into program behavior. Developers of scientific applications can use performance models to pinpoint bottlenecks and evaluate the effectiveness of optimization strategies.

*This work has been submitted to the IEEE for possible publication. Copyright may be transferred without notice, after which this version may no longer be accessible.

On modern computer systems, the floating-point capability of CPUs is often much higher than the data transfer capability of memory. As a result, many kernels, such as Sparse Matrix-Vector Multiplication (SpMV), stencil computations, and vector triad operations along with a wide range of scientific applications, typically encounter memory-bound performance issues. Consequently, developers often rely on performance models such as Roofline Williams et al. [2009] and Execution-Cache-Memory (ECM) Hofmann et al. [2015], which mainly focus on memory and cache bandwidth.

With advances in semiconductor technology, however, processor designs are increasingly narrowing the gap between floating-point throughput and memory bandwidth. For example, consumer CPUs such as the AMD Ryzen 9800X3D integrate large caches, while high performance computing (HPC) processors like the Fujitsu A64FX and Intel Sapphire Rapids employ high-bandwidth memory (HBM). These architectural features reduce the dominance of memory bandwidth, making other design factors, such as pipeline depth, instruction latency, and branch prediction, more influential for application performance. Taking the Fujitsu A64FX as an example: although it is equipped with HBM, its relatively high single instruction multiple data (SIMD) instruction latency (9 cycles for a fused multiply-add operation), together with its small reservation station and limited register file size, constrain its out-of-order (OoO) execution capability. In such cases, application performance is not only limited by memory or cache bandwidth but also by in-core efficiency. Meanwhile, modern workloads are also increasingly arithmetic-intensive. For example, deep learning networks involve a large number of tensor operations that are dominated by arithmetic computation. As a result, in-core execution efficiency has become as important as memory and cache performance.

In scientific software applications, the finite element method (FEM) is one of discretization methods used to solve partial differential equations. The discretization accuracy can be improved by increasing the polynomial order (P) within each element. For multidimensional problems, sum-factorization enables a significant reduction in computational cost when the polynomial expansions posses a tensor-product structure (e.g., in hexahedral elements). This technique is widely regarded as a standard optimization strategy in high-order FEM Bressan and Takacs [2019], Badger et al. [2020]. The core computational kernel of sum factorization is a tensor n -mode product that contains a long inner product within its loop body, and therefore directly encounters the limited OoO execution efficiency issue as described above. Prior work Ren et al. [2025] demonstrated that performance can be improved by splitting this inner product into multiple parts. However, because the length of the inner product varies with P , it is difficult to define a unified splitting strategy. As a result, a trial-and-error approach was used to determine the optimal number of splits and the length of each segment for different polynomial orders. The study suggested that performance degradation arises from data dependencies in the loop body and that splitting alleviates this issue. However a detailed explanation of why splitting improves performance remains missing. Additionally, the trial-and-error process is inefficient for practical tuning, motivating the need for a more systematic and predictive approach.

Developing such a predictive approach faces two main challenges. First, general memory-bandwidth-oriented models such as the standard Roofline model cannot fully explain the performance of our tensor kernel. For example, in the cases studied in Ren et al. [2025], the Bytes per FLOP (B/F) ratios of the tensor kernels for $P = 7$ to $P = 11$ range from 0.7 to 0.5, indicating that the kernel is arithmetic-intensive. On the Fujitsu A64FX processor, whose B/F ratio for L1 cache is 4, the workload's B/F is much smaller than the machine's B/F, implying that the kernel should be compute-bound. Yet, despite this prediction, performance still varies significantly with different loop-body splitting strategies, revealing that bandwidth-oriented models alone cannot capture the instruction-level behavior that governs performance in practice. Second, current analytical models do not incorporate loop-body splitting configurations, such as the number of splits and the length of each segment. These are essential for understanding and predicting the performance changes observed in practice.

Although several frameworks and models for tuning tensor operations vary widely in scope and methodology, they are not directly applicable to our setting. For example, Fang et al. Fang et al. [2017] developed a performance model for tensor operations in deep learning workloads on a specific processor. Although their work mentions instruction-level optimizations, the model primarily emphasizes data transfers across memory, caches, and registers. TVM Chen et al. [2018a], a machine learning-based compilation framework, offers AutoTVM Chen et al. [2018b], an automated tuning system that generates high-performance tensor kernels using statistical cost models with hardware awareness. However, AutoTVM is designed for deep learning workloads and is difficult to apply directly to sum factorization implementations in high-order FEM. Świrydowicz et al. Świrydowicz et al. [2019] proposed a performance model for accelerating tensor products in high-order finite element methods, but their Roofline-like formulation does not capture instruction-level effects. Moreover, commonly discussed tensor-operation optimizations focus on loop tiling or loop reordering. By contrast, loop-body splitting, which is the topic examined in this research, is rarely discussed in the literature.

To address these issues, we first develop a dependency-chain-based analytical model to interpret how loop-body splitting affects performance, particularly on the Fujitsu A64FX processor. We then collect performance data from both the Fujitsu A64FX and Intel Xeon Gold 6230 processors. To enable the realistic performance prediction, the analytical

model with XGBoost Chen and Guestrin [2016], a decision-tree-based machine learning approach, to enable realistic performance prediction. Finally, we compare our results with predictions obtained from the Roofline and ECM models. The contributions of this work are summarized as follows:

- We provide a detailed explanation of loop-body splitting, a less-explored optimization technique that can enhance OoO execution efficiency.
- We propose an analytical model to interpret the performance variation caused by loop-body splitting in tensor n -mode product kernels from the perspective of dependency chains. The analytical model is further extended through a learning-augmented approach that incorporates both machine and code features.
- We demonstrate a promising approach for modeling performance of arithmetic-intensive kernels in scientific computing, which may serve as a useful reference for performance analysis in high-order FEM.

The remainder of this paper is organized as follows. Section II provides the background and motivation for this work. We explain sum factorization and loop-body splitting. Section III introduces the dependency-chain-based model and verifies it using microbenchmarks. Section IV describes the learning-augmented model that builds upon the dependency-chain formulation. Section V evaluates the feasibility and predictive accuracy of the learning-augmented model and compares it with the widely used Roofline and ECM models. Section VI discusses related work. Finally, Section VII concludes the paper and outlines future directions.

2 Background and Motivation

This study uses SCALE-DG Kawai and Tomita [2023, 2025], an atmospheric dynamical core based on the discontinuous Galerkin method (DGM). The DGM is a class of finite element methods. In this section, we introduce how the simulation programs are accelerated through the sum-factorization technique and how additional speedup is achieved by splitting the loop body in the tensor n -mode product kernel. This section provides the background and motivation for the present study.

2.1 Accelerating SCALE-DG via Sum Factorization

The DGM is attractive for HPC because its element-wise formulation localizes most computations within each element, with communication occurring only through fluxes across element interfaces. This property makes the method naturally parallelizable and well suited to distributed-memory architectures. The element-wise independence also reduces the need for global solves, which is a major advantage over continuous finite element methods.

However, the matrix-vector multiplications appear when evaluating the volume and surface terms and applying modal filters. In the general implementations for arbitrary elements, the size of operator matrix is $O((P + 1)^6)$, where P is the polynomial order. As P increases, it becomes extremely large, resulting in substantial computational cost and memory pressure per element. For hexahedral elements, sum factorization is commonly applied to alleviate these issues by exploiting the tensor-product structure of the basis functions. As shown in Fig. 1, sum factorization unfolds the element along each spatial direction and performs a mode- n product with a corresponding one-dimensional operator matrix. This reduces the storage requirement from $O((P + 1)^6)$ to $O(3 \times (P + 1)^2)$, while simultaneously lowering the computational cost.

Fig. 2 shows its execution time for $P = 7$ and $P = 11$ on the Fujitsu A64FX processor. For $P = 7$, the sum factorization reduces it from 1.50 s to 0.125 s, while from 8.52 s to 0.231 s for $P = 11$. These correspond to speedups of $11.9 \times$ and $36.8 \times$, respectively.

2.2 Performance Variation by Splitting the Loop Body

Although the program achieved significant speedups through the application of sum factorization, detailed profiling from previous research Ren et al. [2024] revealed that there is still room for further improvement. That study reported that the tensor n -mode product kernel used in sum factorization suffers from processor pipeline hazards. Listing 1 shows pseudo-code of the tensor n -mode product kernel in the x direction from the sum-factorization-based implementation.

The loop body consists of a long inner product whose number of terms is determined by the polynomial order (P). Each term performs a multiply-add operation, which on modern processors can be executed as a fused multiply-add (FMA) instruction. In the inner product, q_tmp appears on both the left-hand and right-hand sides of each multiply-add operation. Since every new result depends on the updated value of q_tmp , all instructions form a strict data dependency chain. In the processor pipeline, this dependency forces each FMA instruction to wait until the previous one has

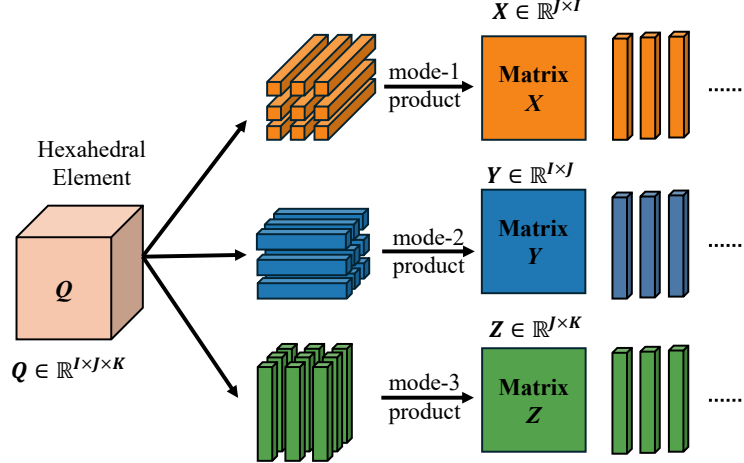
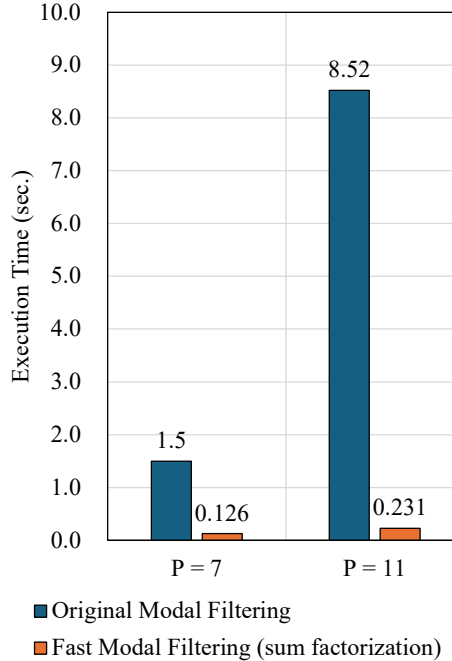


Figure 1: Illustration of sum factorization on hexahedral element.

Figure 2: Execution time of the original and fast modal filtering (sum factorization implemented) at $P = 7$ and $P = 11$ Ren et al. [2024].

completed. The resulting stall time is equal to the instruction latency, which is the fundamental source of the pipeline hazard when the latency is long. Similar patterns occur in the other coordinate directions, leading to the same issue.

In practice, compilers will not typically generate such a naive sequence of dependent instructions. Instead, they often use multiple registers to hold intermediate results and thereby reduce dependency stalls. However, registers and reservation stations in real processors are limited resources. When the instruction sequence becomes very long, the compiler may be forced to reuse registers for accumulation, reintroducing dependency chains and pipeline hazards.

The solution is straightforward: split the inner product in the loop body into multiple parts, as illustrated in the pseudo-code in Listing 2. This approach relaxes data dependencies and improves the efficiency of instruction-level parallelism (ILP).

Listing 1: Pseudo-code of the tensor n -mode product kernel in the x direction.

```

do k=1, Np
do j=1, Np
do i=1, Np
    q_tmp(i,j,k) = mat(i,1) * q(1,j,k) +&
                    mat(i,2) * q(2,j,k) +&
                    mat(i,3) * q(3,j,k) +&
                    mat(i,4) * q(4,j,k) +&
                    mat(i,5) * q(5,j,k) +&
                    mat(i,6) * q(6,j,k) +&
                    mat(i,7) * q(7,j,k) +&
                    mat(i,8) * q(8,j,k) +&
    ! ... ...
end do
end do
end do

```

Listing 2: Pseudo-code of the tensor n -mode product kernel in the x direction with loop-body splitting.

```

do k=1, Np
do j=1, Np
do i=1, Np
    tmp1 = mat(i,1) * q(1,j,k) +&
            mat(i,2) * q(2,j,k) +&
            mat(i,3) * q(3,j,k)
    tmp2 = mat(i,4) * q(4,j,k) +&
            mat(i,5) * q(5,j,k) +&
            mat(i,6) * q(6,j,k)
    tmp3 = mat(i,7) * q(7,j,k) +&
            mat(i,8) * q(8,j,k) +&
    ! ...
    q_tmp(i,j,k) = tmp1 + tmp2 + tmp3 + !...
end do
end do
end do

```

Again, taking the modal filtering process in SCALE-DG as an example, Fig. 3 shows its execution time under different splitting configurations when $P = 8$ on the Fujitsu A64FX processor. Observable performance variations can be clearly recognized from the results, demonstrating that the choice of splitting configuration significantly affects performance.

The ideal splitting configuration would assign the result of each multiply-add operation to distinct variables or registers. However, as mentioned above, the number of registers in a real processor is finite, and the final accumulation step can introduce similar dependency issues if it becomes too long. Therefore, an appropriate splitting strategy must be determined to achieve the best performance. Previous research Ren et al. [2025] used a trial-and-error approach to identify the optimal splitting configuration, including the number of splits and the length of each part.

Since the searching space is not large, the trial-and-error approach was enough to find out the optimal configurations. However, more systematic and predictive approach is useful for practical tunings. This motivated us to propose a model to predict the performance variations and find out the optimal configurations.

3 Dependency Chain-Based Analytical Model

In this section, we first introduce the concept of dependency chain and how we bridge the loop body splitting to the dependency chain. Then we introduce the proposed dependency chain-based analytical model to predict the cycles per instruction (CPI) of the fused multiply-add (FMA) instruction in the tensor n -mode product kernel. Finally, we verify the model with micro-benchmark on both Fujitsu A64FX and Intel Xeon Gold 6230 processors.

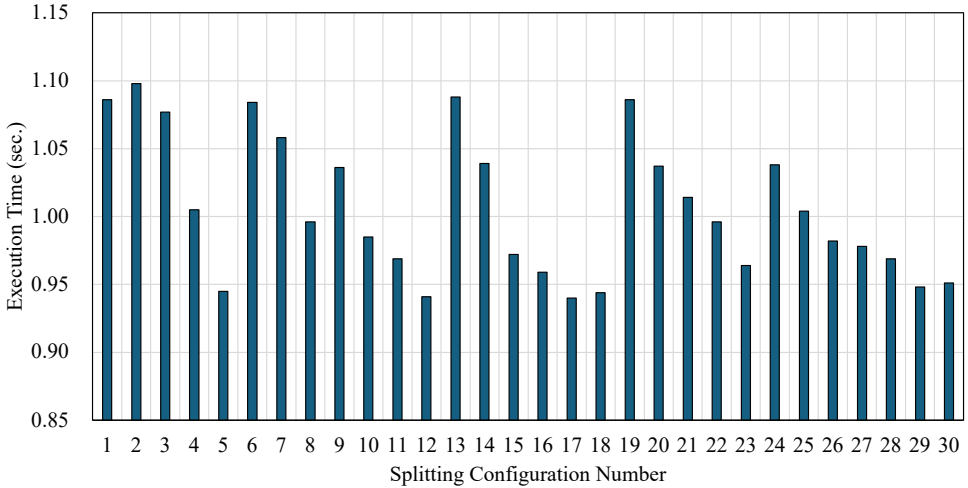


Figure 3: Execution time of the fast modal filtering (sum factorization implemented) at $P = 8$ in different splitting configurations on the Fujitsu A64FX processor Ren et al. [2025].

3.1 Mapping Loop body Splitting to the Dependency Chain

As introduced in Section 2.2, the performance degradation of the tensor n -mode product kernel caused by pipeline hazards can be traced to long data dependency chains in the loop body. The dependency chain, also referred as critical path (CP), is a sequence of instructions in which each depends on the results of the previous ones. The concept of it is not new. It commonly arises in processor architecture design Karkhanis and Smith [2007] and static code analyzers noa [2025]. To illustrate how data dependency chains affect instruction execution time, we provide a highly simplified pipeline model of the floating-point unit (FPU) in Fig. 4.

Modern processors usually include multiple identical functional units to support parallel instruction execution. On the Fig. 4(a), all FMA instructions are independent, allowing each instruction to be dispatched freely to any FPU. In this case, two instructions can be issued and executed per cycle, yielding an average execution time of 0.5 cycles per instruction, which corresponds to the instruction throughput.

By contrast, the Fig. 4(b) depicts a fully data-dependent instruction stream. Although subsequent instructions can, in principle, be dispatched to either FPU0 or FPU1, they must wait until the previous instruction completes. The waiting time is determined by the instruction latency, which on the Fujitsu A64FX processor is 9 cycles for an FMA operation.

In the tensor n -mode product kernel, each term of the inner product is a multiply-add operation and corresponds to an FMA instruction. Figure 5 illustrates the mapping when the loop body contains four multiply-add operations. The splitting configuration consists of two components. The first is the split count N , which indicates how many parts the loop body is divided into. The second is a set $Comb\{l_1, l_2, \dots, l_n \mid 1 \leq n \leq N\}$, referred to as the split-length combination, which specifies how many terms are included in each split.

With a splitting configuration of $N = 1$ and $Comb\{4\}$, no splitting is applied. In this case, the loop body corresponds to a fully data-dependent instruction stream, resulting in long stalls as introduced earlier. In contrast, with a two-way splitting configuration ($N = 2, Comb\{2, 2\}$), the original long dependency chain is transformed into several shorter chains, including the accumulation chain. Although these chains are not modeled individually, the overall effect of two-way splitting is a reduction in the longest dependency depth.

Based on these observations, we can directly bridge the loop-body splitting pattern to the corresponding dependency chains. The execution time of the kernel can then be approximated by examining the execution time of these FMA instructions.

3.2 Model Description

These observations above allow us to construct an analytical model that predicts the execution time of FMA instructions. Fig. 6 illustrates an instruction stream of a tensor n -mode product, which contains multiple data dependency chains. We

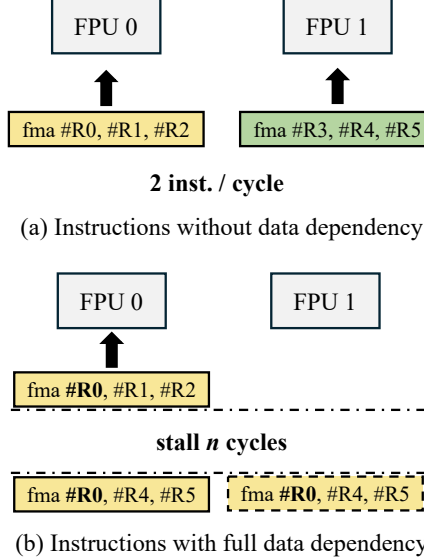


Figure 4: Illustration of floating point arithmetic pipeline status with and without data dependency.

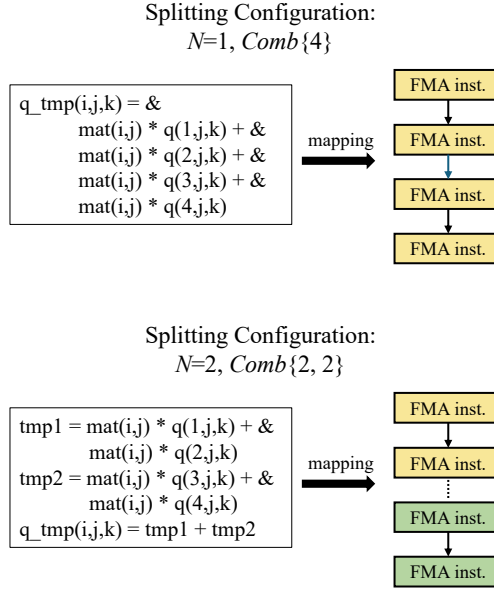
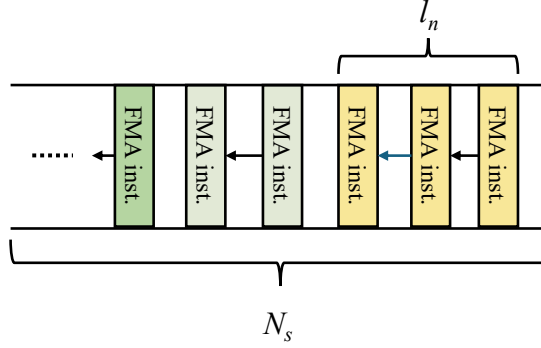


Figure 5: Illustration of mapping loop body splitting configurations to the FMA instruction dependency chains.

denote the total number of instructions in the stream as N_s , and the length of the n th dependency chain as l_n which is directly determined by the split-length combination. The execution time of each FMA instruction is assumed to be dominated by the longest dependency chain. Accordingly, Equation (1) defines the ratio between the length of the longest dependency chain and the total length of the instruction stream:

$$Ratio = \frac{\max\{l_1, l_2, \dots, l_n\}}{N_s} \quad (1)$$

This ratio reflects the fraction of instructions that are constrained by dependency chains, as opposed to those that can execute at the architectural throughput. A ratio close to zero corresponds to a throughput-bound case, whereas a ratio close to one corresponds to a latency-bound case. Since loop-body splitting directly shortens dependency chains, different splitting configurations are naturally represented by variations in this ratio. Only the longest dependency chain



N_s : Number of the instructions in the stream.

l_n : Length of the n -th dependency chain.

Figure 6: Definition of N_s and l_n in the instruction stream.

Table 1: FMA instruction throughput and latency (in cycles) of the Fujitsu A64FX and Intel Xeon Gold 6230.

	$T_{throughput}$	$T_{latency}$
Fujitsu A64FX	0.5	9
Intel Xeon Gold 6230	0.5	4

is considered, because the execution time of an instruction stream is determined by the execution time of the longest chain, as concluded by Michaud et al. Michaud et al. [2001].

The average execution time T_{FMA} of each FMA instruction can then be calculated using Equation (2):

$$T_{FMA} = \text{Ratio} \times T_{latency} + (1 - \text{Ratio}) \times T_{throughput} \quad (2)$$

Here, $T_{latency}$ represents the latency of an FMA instruction, while $T_{throughput}$ denotes the throughput of FMA instructions. Both values depend on the processor's pipeline design and the number of FPUs.

This model is valid under the following assumptions:

- The data transfer time is overlapped by computation.
- FMA instructions dominate the instruction stream.

3.3 Verification with Microbenchmark

A microbenchmark was developed to validate the analytical model. As shown in Fig. 7, five patterns are evaluated in this benchmark. Patterns A and D represent the pure throughput and full-latency conditions, respectively. Pattern B represents the case with two dependency chains of equal length. Pattern C represents a single dependency chain together with one independent instruction. Finally, Pattern E represents two dependency chains with different lengths. The values of N_s and l_n for each pattern are also provided in the Fig. 7.

Two processors are used for verification: the Fujitsu A64FX and the Intel Xeon Gold 6230. The FMA instruction throughput and latency are summarized in Table 1. For the A64FX, the instruction characteristics are obtained from its microarchitecture manual noa [a]. The Intel Xeon Gold 6230, based on the Cascade Lake architecture, is characterized using data from uops.info Abel and Reineke [2019]. Both processors feature two floating-point units, giving an instruction throughput of 0.5 cycles per FMA. However, the A64FX exhibits a higher latency of 9 cycles compared to the Intel Xeon, due to differences in pipeline design.

To evaluate execution time at the CPU cycle level, we use information from counter timer registers for more precise measurements. On the Fujitsu A64FX, cycle counts are obtained from the CNTVCT_ELO register via the mrs instruction. Since this register operates at its own sampling frequency, the true CPU clock cycles must be recovered by reading the frequency from the CNTFRQ_ELO register. Our A64FX runs at 2.2 GHz, so the actual CPU cycles of the benchmark program can be computed using Equation (3):

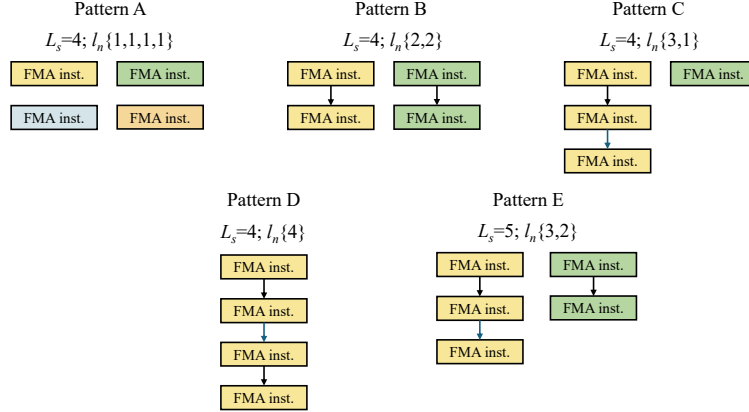


Figure 7: Dependency chain patterns used in the microbenchmark.

Table 2: Estimated and measured execution Time (in cycles) of the 5 dependency patterns on the Fujitsu A64FX and Intel Xeon Gold 6230 processors.

Pattern	Ratio	Fujitsu A64FX		Intel Xeon Gold 6230	
		Estimated T_{FMA}	Measured T_{FMA}	Estimated T_{FMA}	Measured T_{FMA}
A	0.0	0.50	0.50	0.50	0.53
B	0.50	4.8	4.5	2.3	2.0
C	0.75	6.9	6.8	3.1	3.0
D	1.0	9.0	9.0	4.0	4.0
E	0.60	5.60	5.4	2.6	2.4

$$T_{microbench} = cntvct_cycles \times \frac{CPU_frequency}{cnvct_frequency} \quad (3)$$

The execution time (in cycles) of each FMA instruction is then obtained by dividing $T_{microbench}$ by the number of instructions in the microbenchmark program. On the Intel Xeon processor, the same approach is applied, but cycle counts are obtained using the `__rdtsc` intrinsic. Equation (3) is again used to compute cycles. However, because Intel CPUs support dynamic frequency scaling (turbo boost), determining the actual CPU frequency is less straightforward and requires profiling tools such as VTune.

Table 2 shows the results of the estimated and measured execution time per FMA instruction for all five patterns. The dependency chain-based analytical model estimated very close values compared with the measured values in pattern A and D which are pure throughput and full-latency conditions, respectively, despite which processor it is. On both processors, the estimated execution time per FMA in pattern B, C, and E is slightly higher than the real measurements. It is because the $T_{throughput}$ term in the model, where in actual execution the shorter terms in pattern B, C, and E can be overlapped by the longer terms.

3.4 Limitations of the analytical dependency chain-based model

Although the analytical dependency-chain model explains the performance variations caused by loop-body splitting in the tensor mode- n product of SCALE-DG and performs well on the microbenchmark program, it is difficult to apply it directly to real applications for the following reasons:

- Register usage is restricted in the benchmark program, whereas in real programs more registers are available. Moreover, in the benchmark the dependency chains are arranged in a regular order, but in practice, due to OoO execution, the actual instruction stream may appear chaotic. This makes it difficult to identify the maximum l_n manually.
- Compilers apply a variety of optimization techniques such as loop unrolling and software pipelining (SWP), which affect the final instruction scheduling. As a result, the actual length of the instruction stream (N_s) is uncertain.

Since both factors needed to calculate the *Ratio* are uncertain, it is challenging to use the analytical model directly for performance prediction, especially for kernels with a large instruction base. To make the model more practical, two approaches may overcome this limitation: (1) using static code analysis tools to extract information from the kernel’s assembly code, or (2) applying machine learning to predict the *Ratio*.

4 Learning-Augmented Performance Model

In this section, we introduce a machine learning–based approach to overcome the limitations of the analytical model and make it more practical. First, we define a target function for machine learning, and then we describe the feature design and model structure.

4.1 Target Function

In the original analytical model, the average execution time per FMA (T_{FMA}) depends on the dependency ratio as shown in Equation (1). However, as discussed in Section 3.4, directly calculating this ratio is challenging due to compiler optimizations and OoO execution. We therefore define the learning target as the dependency ratio:

$$Ratio = f(code_features, hardware_features) \quad (4)$$

The input features comprise both machine-level characteristics and code-level features. The calculation of T_{FMA} still follows Equation (1), so the new model operates in a hybrid manner. Since all ratios fall within the range $[0, 1]$, they can be regarded as probability-like values. While they are not true probability distributions, this bounded shape makes them more suitable for regression compared with predicting kernel-level giga floating-point operations per second (GFLOPS) or execution time directly.

The concept of constructing performance models based on both code and processor features dates back to the early stages of performance modeling research. The work of Noonburg et al. [1994] proposed a theoretical model for ILP. They decomposed ILP into program parallelism, which corresponds to control and data dependencies, and machine parallelism, which corresponds to factors such as branch prediction and instruction issue policies. This framework closely resembles the principles adopted in later research, including our own approach.

Furthermore, while much research on interpretable AI (e.g., XAI Ali et al. [2023] or SHAP values Lundberg and Lee [2017]) focuses on extracting explanations from black-box predictors, our approach is inherently more transparent because it is grounded in an analytical model. By choosing the dependency ratio as the learning target, the machine learning model complements rather than replaces the analytical formulation, thereby preserving the interpretability of the latency/throughput decomposition. At the same time, this design makes the model more robust to compiler scheduling effects and more generalizable to other arithmetic-intensive kernels.

4.2 Features and Model Design

Table 3 summarizes the details of the code and hardware features. The code features are intended to represent the characteristics of the tensor n -mode product as completely as possible. Np denotes the degrees of freedom (DoF) along one dimension, determined by the polynomial order (P) as $P + 1$. FLOPs represents the total number of floating-point operations in the kernel, which varies with P . Since the loop iterations and the terms in the loop body are known before execution, this quantity is straightforward to calculate. The split count and split-length combinations, introduced in Section 3.1, are key factors linking instruction dependency chains to the code implementation.

The hardware features include CPU frequency, the latency and throughput of FMA instructions, the number of FPU in the CPU, and the supported vector length. The reservation station size is a more esoteric parameter, and not all processor manuals provide this information. If it is unavailable, it can be treated as a missing value in the machine learning model.

All features and target values can be represented as a row in a tabular dataset. For learning from such data, XGBoost (eXtreme Gradient Boosting) Chen and Guestrin [2016] is a well-suited choice. XGBoost is a tree-based machine learning framework that applies gradient boosting. We employ XGBoost instead of more complex models such as deep neural networks because our dataset size is relatively modest, and tree-based boosting methods are known to achieve high accuracy in such settings without overfitting.

Moreover, while deep learning approaches often function as opaque black boxes, XGBoost maintains interpretability through feature importance metrics, which is essential for explaining how code and hardware features influence performance. XGBoost is also efficient, because both training and inference are lightweight, making the model practical

Table 3: Code and hardware features for the learning target.

Code features	Np FLOPs Split Count: N Split-length Combination: $Comb\{\dots\}$
Hardware features	Frequency FMA latency FMA throughput FPU numbers Vector Length Register Number Reservation Station Size

Table 4: Specifications of Fujitsu A64FX and Intel Xeon Gold 6230.

	Fujitsu A64FX	Intel Xeon Gold 6230
Frequency (GHz)	2.2	2.0 (all-core AVX-512)
Floating Point Units	2	2
Floating Point Registers	128 entries	168 entries
Reservation Station	40 entries	97 entries
Vector ISA extensions	SVE	AVX-512
Vector Length (bits)	512	512
L1 Cache	64 KiB	32 KiB
Cores	48	20
NUMAs (CMGs)	4	1

to integrate with existing performance-analysis workflows. Finally, because the regression target is the dependency ratio defined in Equation (4), XGBoost complements rather than replaces the analytical model, ensuring that the latency/throughput decomposition remains intact.

5 Evaluation

In this section, we describe how the training data were prepared and how the training procedure was conducted. We then present the training results and compare them with the Roofline and ECM models.

5.1 Experimental Setup

The evaluation is conducted on the Fujitsu A64FX and Intel Xeon Gold 6230 processors. Hardware specifications are listed in Table 4. Our Fujitsu A64FX runs in boost mode, with a frequency of 2.2 GHz. The Intel Xeon processor supports dynamic frequency scaling; however, on the Cascade Lake architecture the frequency is locked at 2.0 GHz when running full-core AVX-512 code.

To collect training data, we developed a mini-application that implements only the tensor n -mode product. On the A64FX platform, the Fujitsu profiling tool was used to collect performance data, while on the Intel Xeon platform, the Performance Application Programming Interface (PAPI) Jagode et al. [2025] was employed. The tensor n -mode product for a single element is too small to be measured accurately with these profilers. In addition, FEM computations perform the tensor n -mode product over the elements assigned to each CPU core. For these reasons, the mini-application handles tensor n -mode products executed over multiple elements. As performed in SCALE-DG, OpenMP was used to parallelize the element-level loop. One Core Memory Group (CMG) was utilized on the A64FX processor, while a single NUMA node (20 cores) was used on the Intel Xeon processor. Computations within the element are vectorized using 512-bit SVE instructions on the A64FX processor and AVX-512 instructions on the Intel Xeon processor.

For comparison with the ECM model, we applied the static code analysis tool `l1vm-mca noa [b]` for in-core evaluation. Although the original ECM studies typically employed OSACA noa [2025] as the in-core analysis tool, we found that OSACA performed poorly on large instruction sequences. For example, the tensor n -mode product at $P = 7$ produces an assembly file of 5,000–6,000 lines due to full loop unrolling by the Fujitsu compiler. On such input, OSACA ran very slowly and did not generate reasonable results. In addition, OSACA lacks support for some specific Arm SVE

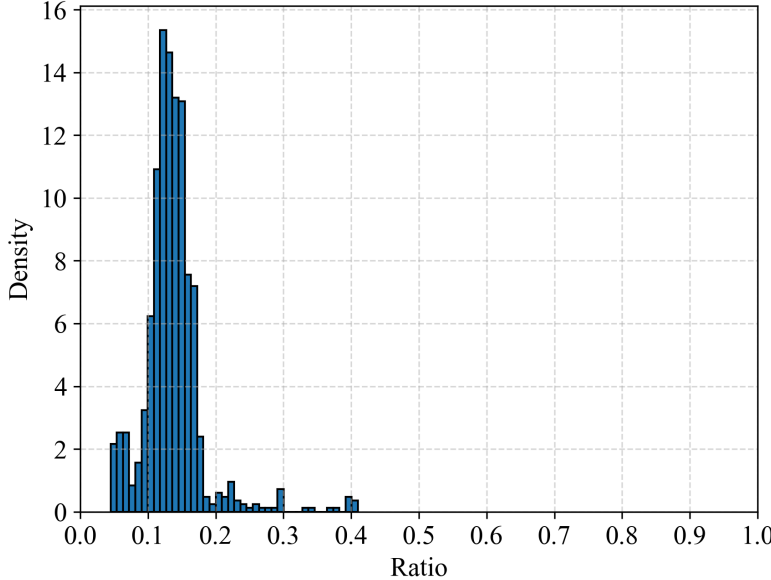


Figure 8: Distribution of $Ratio$ on the Fujitsu A64FX ($1 \leq P \leq 15$).

instructions. By contrast, although the developers of `l1vm-mca` state that it is not intended for predicting execution time, we found it to perform well under our conditions.

5.2 Training Data and Procedure

Performance data for all split-length combinations with polynomial order P ranging from 1 to 15 were collected on the Fujitsu A64FX and Intel Xeon Gold 6230, yielding approximately 1,800 rows of data. The dependency ratio ($Ratio$) was computed retrospectively from the collected GFLOPS per core, instruction counts, processor frequencies, and instruction throughput and latency values. The detailed method is described in Appendix A.

It should be noted that for $P = 15$ on the Intel Xeon Gold 6230, the kernel’s data size is about 70 KiB, which greatly exceeds the processor’s L1 cache capacity (32 KiB). In some cases, the calculated $Ratio$ values were greater than 1.0, which is unexpected. This may indicate that the data transfer time cannot be fully overlapped by the computation time, thereby violating the model’s assumption stated in Section 3.2. Therefore, the data corresponding to $P = 15$ on the Intel Xeon Gold 6230 were excluded from the training dataset. However, these data were still used in the results and analysis section for comparison with the ECM and Roofline models. In total, approximately 1,500 rows of data were used for training and validation.

Before training, we plotted the distribution of the dependency ratio ($Ratio$) to verify whether it exhibits the probability-like behavior assumed in Section 4.1. Fig. 8 shows the distribution on the Fujitsu A64FX. The ratios approximate a normal-like distribution, with values falling in the range [0.05, 0.4] and most concentrated in [0.1, 0.2]. Fig. 9 shows the distribution on the Intel Xeon processor. In contrast to the A64FX, the ratio distribution on the Xeon exhibits greater variance, with three distinct peaks appearing around 0.1, 0.2, and 0.3.

For the training procedure, we used the `XGBRegressor`, a widely adopted regression library based on XGBoost. The dataset was split into 80% for training and 20% for testing. Model hyperparameters were tuned using the `RandomizedSearchCV` function in the `scikit-learn` library.

5.3 Results and Discussion

Fig. 10 shows a scatter plot comparing the predicted dependency ratio with the measured ratio. The closer the points lie to the diagonal line, the better the prediction quality. As indicated by the data distributions in Fig. 8 and Fig. 9, most ratios fall within the range [0.05, 0.4], and in this range Fig. 10 shows good agreement between prediction and

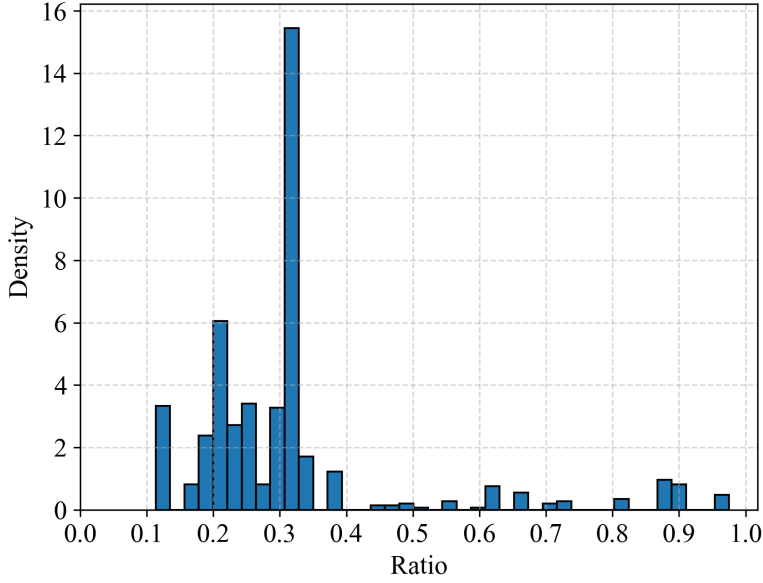


Figure 9: Distribution of $Ratio$ on the Intel Xeon Gold 6230 ($1 \leq P \leq 14$).

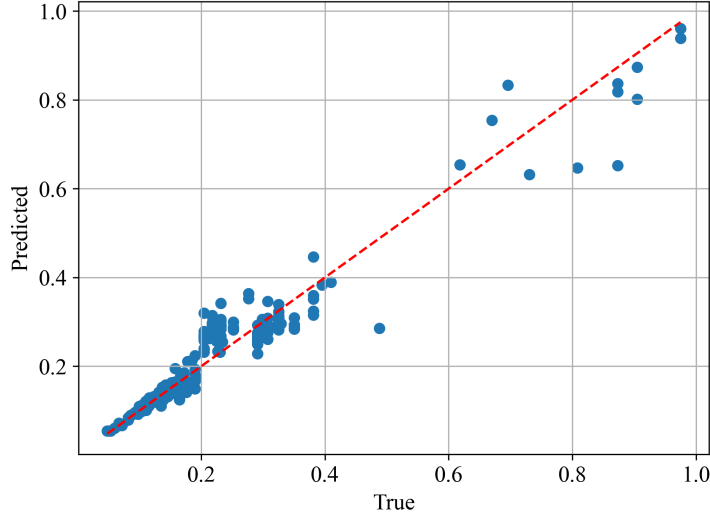


Figure 10: Training result of the learning target.

measurement. However, in the range $[0.6, 1.0]$, the results deviate significantly from the diagonal line, primarily due to insufficient training samples in this region.

Because the dependency ratio itself is not intuitive, we converted it into GFLOPS and compared our results with those of the widely used Roofline and ECM models. The detailed procedures for estimating GFLOPS with Roofline and ECM are provided in Appendix B. Fig. 11 shows the GFLOPS estimated by Roofline, ECM, and our learning-augmented model for test cases on the A64FX at polynomial order $P = 7$. The lateral axis represents different split-length combinations. The results show that both the Roofline and ECM models overestimate kernel performance, while our model produces values much closer to the measurements.

Fig. 12 illustrates the same comparison on the Intel Xeon processor. In this case, the ECM model consistently predicts higher GFLOPS than the Roofline model. This is because the Roofline model bases its prediction solely on memory

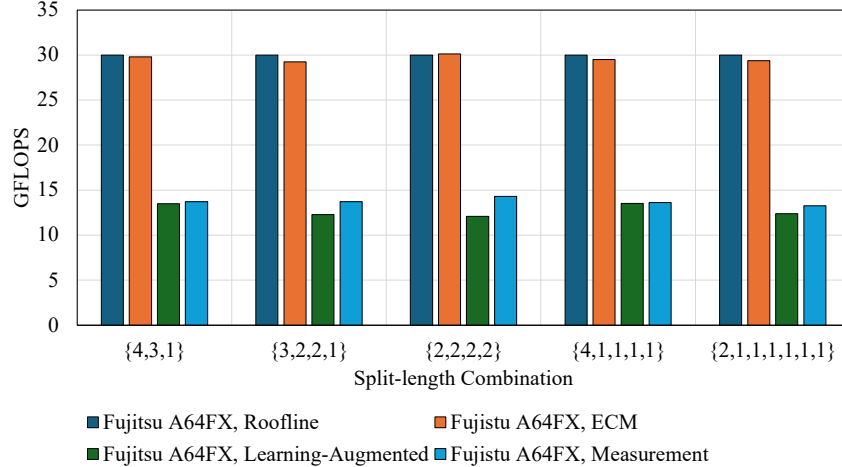


Figure 11: GFLOPS per core at $P = 7$ estimated by the Roofline, ECM, and Learning-Augmented models compared to the measured values on the Fujitsu A64FX.

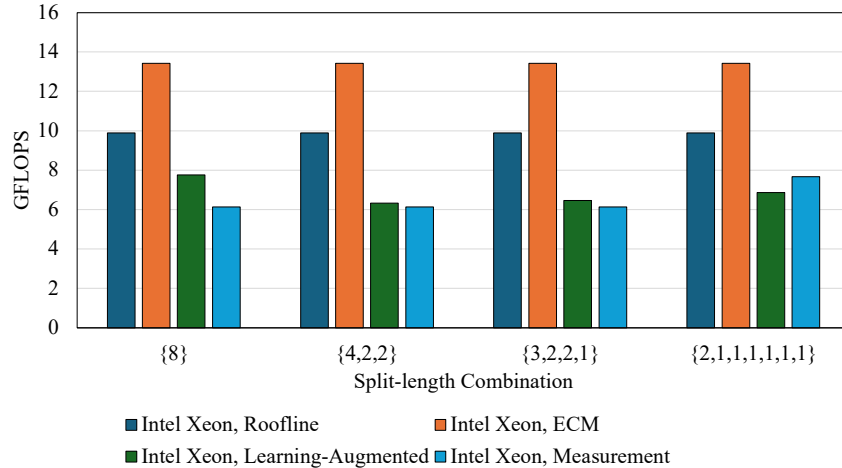


Figure 12: GFLOPS per core at $P = 7$ estimated by the Roofline, ECM, and Learning-Augmented models compared to the measured values on the Intel Xeon Gold 6230.

bandwidth, whereas the ECM model also accounts for data transfers at each cache level. Since in our experiments almost all hot data reside in the L1 cache, whose bandwidth is substantially larger than main memory, the ECM model reports higher GFLOPS than Roofline. Nevertheless, neither Roofline nor ECM closely matches the real measurements, whereas the learning-augmented model does.

To compare the learning-augmented model with the ECM and Roofline models across different polynomial orders (P) and splitting configurations, Fig. 13 and Fig. 14 are provided. Fig. 13 shows the mean absolute percentage error (MAPE) of GFLOPS predicted by the learning-augmented, Roofline, and ECM models compared with the measured values, grouped by P on the Fujitsu A64FX processor. The data are from the 20% testing subset, the vertical axis is presented in logarithmic scale. The learning-augmented model demonstrates excellent prediction accuracy across all P values, with errors ranging from 1% to 24%. The Roofline model exhibits larger errors but shows reasonable agreement at $P = 5$. The ECM model performs better than the Roofline model, providing very accurate predictions for $P = 1, 2$ and $P = 8, 9, 10$. This occurs because, for $P = 1, 2$, the data transfer volume is too small for memory effects to dominate, so the in-core execution time estimated by `l1vm-mca` governs the total performance. For $P = 8, 9, 10$, the data size causes the data transfer time to become comparable to the in-core execution time. Overall, however, the learning-augmented model outperforms the ECM model in predictive accuracy.

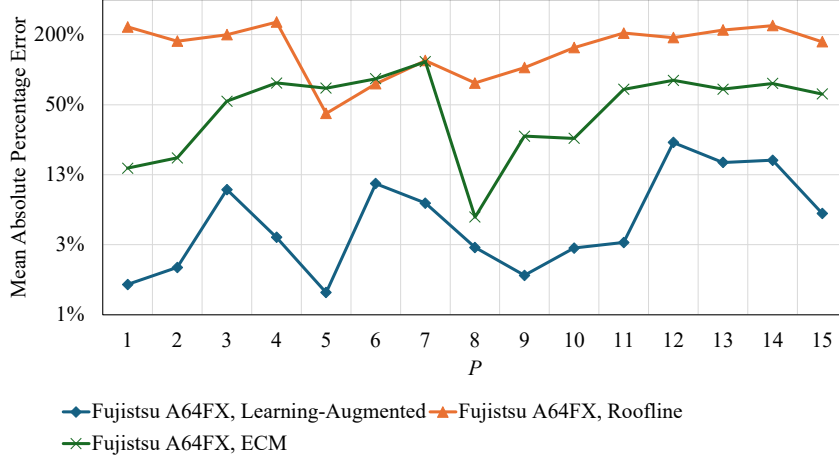


Figure 13: Comparison of Learning-Augmented, Roofline, and ECM model across different P s and split-length combinations on the Fujitsu A64FX.

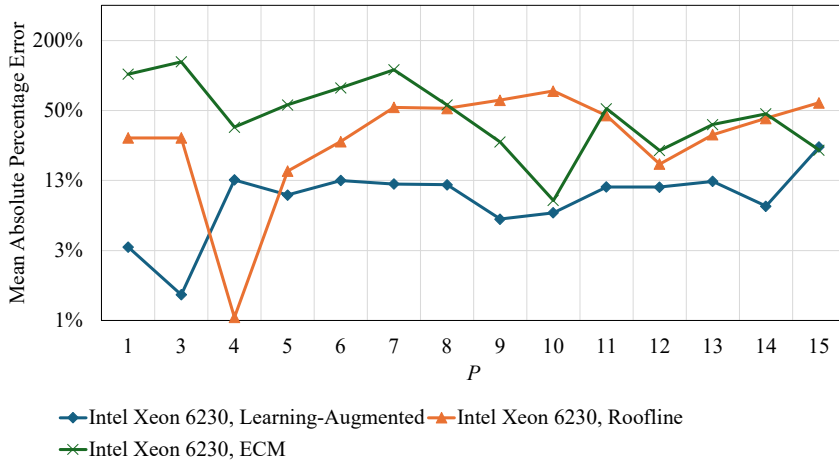


Figure 14: Comparison of Learning-Augmented, Roofline, and ECM model across different P s and split-length combinations on the Intel Xeon Gold 6230.

Fig. 14 shows the same MAPE comparison, this time on the Intel Xeon Gold 6230 processor. The learning-augmented model again demonstrates excellent overall performance for $P = 1$ to $P = 14$, with prediction errors ranging from 1% to 13%. Interestingly, the Roofline model exhibits smaller errors than the ECM model in many cases, opposite to the trend observed on the A64FX, and even provides highly accurate predictions at $P = 4, 5$. The ECM model shows larger errors than the Roofline model in most cases, primarily because its estimated performance is based on cache bandwidth which has been stated when describing results in the Fig. 12. As a result, the Roofline predictions are typically lower than those of the ECM model. Nevertheless, the ECM model provides very good predictions at $P = 9, 10$, and 12.

A particularly noteworthy case in Fig. 14 is at $P = 15$, where the data violate the assumptions of our learning-augmented model. The MAPE of the learning-augmented model is slightly above 20%, representing a noticeable degradation compared with predictions at other P values. In this regime, data transfers between memory hierarchies can no longer be ignored, and this is precisely the situation that the ECM model is designed to handle. Although the MAPE is around 20%, a direct comparison of absolute GFLOPS provides additional insight: the measured performance is approximately 12–15 GFLOPS, while the ECM model predicts about 15 GFLOPS and the learning-augmented model predicts 10–11 GFLOPS. Consequently, in this case, the ECM model demonstrates superior accuracy.

5.4 General Application Performance Modeling

For general application performance evaluation, widely used models such as the standard Roofline model Williams et al. [2009] and the Cache-Aware Roofline model Ilic et al. [2014] primarily focus on memory and cache bandwidth. The Roofline model has been extended by Cabezas et al. Cabezas and Puschel [2014] to incorporate microarchitectural constraints, but dependency-chain or critical-path analysis is usually handled by static code analyzers such as llvm-mca noa [b], which performs cycle-by-cycle simulations of the processor pipeline, and tools such as OSACA Laukemann et al. [2018, 2019] and Facile Abel et al. [2023], which construct analytical throughput models based on static instruction analysis. Although effective, these tools require detailed assembly-level information, which limits their applicability for high-level kernel modeling.

The Execution-Cache-Memory (ECM) model Hofmann et al. [2015] extends the Roofline framework by integrating in-core execution with data transfer modeling across memory hierarchy levels. However, its in-core predictions still rely on throughput estimations from the aforementioned tools. More recent research has begun to incorporate instruction throughput more explicitly. For example, Leinhauser et al. Leinhauser et al. [2021] proposed an Instruction Roofline model for AMD GPUs, and Ding et al. Ding et al. [2022] introduced a similar model for NVIDIA GPUs. Shi et al. Shi et al. [2026] examined the performance impact of Arm’s Scalable Vector Extension (SVE) instructions on HPC processors and proposed a machine learning-based model to classify performance bottlenecks.

5.5 Tensor Operation Performance Tuning

In the more specific domain of tensor operation performance tuning, memory bandwidth remains the dominant evaluation factor. Swirydowicz et al. Świrydowicz et al. [2019] presented a Roofline-like model to evaluate tensor kernels on GPU, incorporating both global and shared memory bandwidth across different polynomial orders. Vectorization efficiency was studied by Kempf et al. Kempf et al. [2021], who developed an automatic framework for generating and tuning tensor operation code in discontinuous Galerkin methods. Their model used a logarithmic function to represent ILP efficiency.

Learning-based performance tuning has also gained attention. Chen et al. Chen et al. [2018b] proposed domain-specific statistical cost models to guide tensor operation optimization in deep learning workloads, using features extracted from low-level abstract syntax trees (ASTs). Kaufman et al. Kaufman et al. [2021] introduced a graph neural network (GNN)-based model for tensor program tuning on Tensor Processing Units (TPUs), outperforming conventional methods for tile-size selection and operator fusion. Similarly, Zhai et al. Zhai et al. [2023] developed a deep learning-based cost model that extracts features from schedule primitives in TVM Chen et al. [2018a]. More recently, Sudusinghe et al. Sudusinghe et al. [2025] proposed a transfer learning-based cost model for sparse tensor operation tuning, which reduces the need for large training datasets. Although these learning-based works do not explicitly model instruction throughput, the code features they use likely encode instruction-level efficiency implicitly.

5.6 Positioning of This Work

Our work shares similarities with learning-based performance models in that it takes both code and hardware features as input and employs XGBoost as the regression model. However, it differs from prior work in several key aspects:

- Unlike purely analytical or purely learning-based approaches, our learning-augmented model adopts a hybrid design to predict the cycles per FMA instruction (CPI). The analytical component ensures interpretability, while the machine learning component enhances robustness and practical applicability.
- While common methods to improve OoO execution include loop unrolling and loop reordering, our work focuses on loop-body splitting, a less explored optimization technique. The proposed model explicitly incorporates split counts and combinations as input features.
- Most ML-based tensor performance tuning studies originate from deep learning frameworks. In contrast, our work focuses on tensor n -mode product in high-order FEM, representing a different application domain.

6 Conclusion

In this study, we proposed a dependency chain-based analytical model to explain the performance variation observed during the optimization of tensor product factorization in high-order FEM, specifically the effect of splitting the loop body. The analytical model bridges the relationship between split counts, split-length combinations, and the data dependencies of FMA instructions in tensor n -mode product implementations. We then augmented the analytical model using XGBoost, creating a learning-augmented approach that enhances robustness and predictive capability.

Evaluation was conducted on the Fujitsu A64FX and Intel Xeon Gold 6230 processors for polynomial orders (P) ranging from 1 to 15. On the A64FX processor, the learning-augmented model achieved a mean absolute percentage error (MAPE) between 1% and 24%, compared with 5%–117% for the ECM model and 42%–256% for the Roofline model. On the Intel Xeon processor, the learning-augmented model achieved MAPE values from 1% to 13% for $P = 1$ –14, increasing to 24% at $P = 15$ due to violation of the model’s L1-cache-residency assumption. The ECM model’s errors ranged from 8% to 112%, while the Roofline model ranged from 1% to 73%. Overall, the learning-augmented model demonstrated consistently superior predictive accuracy across both architectures and most polynomial orders.

This work provides a more systematic approach for tensor product factorization performance tuning in high-order FEM and offers potential applicability to other element-based atmospheric simulation codes, such as SCALE-DG.

In future work, we plan to expand the dataset by collecting data from a wider variety of processors and compilers. Moreover, additional instruction types beyond FMA will be integrated into the model, and cache-related effects, such as miss rates and associated latencies, will be incorporated through predictive modeling.

Acknowledgment

This work was financially supported by JST SPRING, Grant Number JPMJSP2125. This work was also supported by the Joint Usage/Research Center for Interdisciplinary Large-scale Information Infrastructures (JHPCN) and the High-Performance Computing Infrastructure (HPCI) under project number jh250015 and jh250018. In addition, this research was funded by JSPS KAKENHI Grants JP23K11126 and JP24K02945. The author (Initial) would like to take this opportunity to thank the “THERS Make New Standards Program for the Next Generation Researchers”.

Appendices

A Computing dependency ratio retrospectively

Although the profiling tools cannot obtain the dependency ratio directly, we can compute it retrospectively. First, the total execution time in cycles of the kernel is derived using Equation (A.1):

$$T_{kernel} = \frac{FLOPs \times CPU_frequency}{GFLOPS} \quad (A.1)$$

where FLOPs refers to the total floating-point operations of the kernel, GFLOPS refers to the giga floating-point operations per second that obtained from the profilers.

In our model, it is assumed that nearly all execution time is dominated by FMA instructions. Therefore, T_{kernel} can be approximated as the total execution time of all FMA instructions. If the number of FMA instructions is known, the average execution time (in cycles) per FMA can be calculated using Equation (A.2), where N_{FMA} denotes the FMA instruction count:

$$T_{FMA} = \frac{T_{kernel}}{N_{FMA}} \quad (A.2)$$

In this work, if the kernel is fully unrolled, N_{FMA} is obtained by counting the number of FMA instructions in the assembly files. Otherwise, the N_{FMA} is calculated by the the number of FMA instructions in the assembly files times the loop iterations.

Finally, since the instruction throughput and latency of the processor are given, the dependency ratio can be computed using Equation (A.3):

$$Ratio = \frac{T_{FMA} - T_{throughput}}{T_{latency} - T_{throughput}} \quad (A.3)$$

B Estimating GFLOPS using Roofline and ECM model

B.1 Estimating with Standard Roofline model

In this work, the standard Roofline model Williams et al. [2009] is employed to estimate the GFLOPS of the tensor n -mode product. Arithmetic intensity (AI), also called FLOPs per byte, is the only factor required in this model. We consider only the data read and written at the kernel level. The tensor n -mode product reads the hexahedral element data q_in and q_tmp , each of size $(P + 1)^3$, and then writes back the updated element data q_in and q_tmp . The three operator matrices, each of size $(P + 1)^2$, are relatively small compared with the element data and are loaded only

once during the first execution. These matrices are assumed to remain resident in the cache, so their data transfer is ignored. All data are stored in double precision (8 bytes per entry).

The AI can be computed as follows:

$$AI = \frac{FLOPs}{(P+1)^3 \times 4 \times 8} \quad (B.1)$$

The estimated GFLOPS can then be obtained by multiplying AI with the available memory bandwidth. Finally the standard Roofline model can be represented as:

$$GFLOPS \leq \min \begin{cases} \text{Peak} & GFLOPS \\ \text{Peak} & GB/s \times AI \end{cases} \quad (B.2)$$

B.2 Estimating with ECM Model

The ECM model is more complex. It consists of two main components: the execution time that can be overlapped (e.g., in-core arithmetic) and the execution time that cannot be overlapped, including data transfer times. Following the work of C. Alappat et al. Alappat et al. [2022], the basic form of the ECM model on the Fujitsu A64FX is given in Equation (B.3):

$$T_{ECM} = \max\{T_{c_OL}, f(T_{L1_LD}, T_{L1_ST}, T_{L2}, T_{Mem})\} \quad (B.3)$$

Here, T_{c_OL} mainly refers to floating-point operations that can overlap with data transfers. The function $f(T_{L1_LD}, T_{L1_ST}, T_{L2}, T_{Mem})$ represents the data transfer time, which can behave differently depending on the processor. Transfers between different memory hierarchies may or may not overlap, depending on the overlap hypothesis of the processor. For the A64FX, the overlap hypothesis follows Equation (B.4) which also comes from the work Alappat et al. [2022]. For the Intel Xeon Gold 6230 (Cascade Lake), we did not find a precise description of the hypothesis in the literature, but we identified an equation from the official GitHub repository noa [c] of ECM model. We slightly modified it by eliminating the $L1_shared_bw$ term, because in our kernel reads dominate writes, especially at high polynomial orders. In this paper, its overlap hypothesis is expressed by Equation (B.5).

$$f(T_{L1_LD}, T_{L1_ST}, T_{L2}, T_{Mem}) = \max\{T_{L1_LD} + \max\{T_{L1_ST}, T_{L2}\}, T_{Mem}\} \quad (B.4)$$

$$f(T_{L1_LD}, T_{L1_ST}, T_{L2}, T_{L3_RD}, T_{L3_WR}, T_{Mem}) = \max\{T_{L1_LD}, T_{L1_ST}\} + T_{L2} + \max\{T_{L3_RD}, T_{L3_WR}\} + T_{Mem} \quad (B.5)$$

As introduced in Section 5.1, T_{c_OL} , T_{L1_LD} , and T_{L1_ST} are obtained from the static analysis tool `l1vm-mca`. Other execution times are computed by dividing the data transfer volume by the corresponding bandwidth. The estimated single-core GFLOPS is then calculated using Equation (B.6):

$$GFLOPS = \frac{FLOPs}{T_{ECM}} \times CPU_frequency \quad (B.6)$$

References

Samuel Williams, Andrew Waterman, and David Patterson. Roofline: an insightful visual performance model for multicore architectures. *Communications of the ACM*, 52(4):65–76, April 2009. ISSN 0001-0782, 1557-7317. doi:10.1145/1498765.1498785. URL <https://doi.acm.org/doi/10.1145/1498765.1498785>.

Johannes Hofmann, Jan Eitzinger, and Dietmar Fey. Execution-Cache-Memory Performance Model: Introduction and Validation, 2015. URL <https://arxiv.org/abs/1509.03118>. Version Number: 3.

Andrea Bressan and Stefan Takacs. Sum factorization techniques in Isogeometric Analysis. *Computer Methods in Applied Mechanics and Engineering*, 352:437–460, August 2019. ISSN 00457825. doi:10.1016/j.cma.2019.04.031. URL <https://linkinghub.elsevier.com/retrieve/pii/S0045782519302348>.

Jacob Badger, Stefan Henneking, and Leszek Demkowicz. Sum factorization for fast integration of DPG matrices on prismatic elements. *Finite Elements in Analysis and Design*, 172:103385, May 2020. ISSN 0168874X. doi:10.1016/j.finel.2020.103385. URL <https://linkinghub.elsevier.com/retrieve/pii/S0168874X1930722X>.

Xuanzhengbo Ren, Yuta Kawai, Hirofumi Tomita, Seiya Nishizawa, Takahiro Katagiri, Tetsuya Hoshino, Daichi Mukunoki, Masatoshi Kawai, and Toru Nagai. Performance Evaluation of Loop Body Splitting for Fast Modal Filtering in SCALE-DG on A64FX. In *Proceedings of the 2025 International Conference on High Performance Computing in Asia-Pacific Region Workshops*, pages 36–44, Hsinchu Taiwan, February 2025. ACM. ISBN 979-8-4007-1342-2. doi:10.1145/3703001.3724385. URL <https://dl.acm.org/doi/10.1145/3703001.3724385>.

Jiarui Fang, Haohuan Fu, Wenlai Zhao, Bingwei Chen, Weijie Zheng, and Guangwen Yang. swDNN: A Library for Accelerating Deep Learning Applications on Sunway TaihuLight. In *2017 IEEE International Parallel and Distributed Processing Symposium (IPDPS)*, pages 615–624, Orlando, FL, USA, May 2017. IEEE. ISBN 978-1-5386-3914-6. doi:10.1109/IPDPS.2017.20. URL <http://ieeexplore.ieee.org/document/7967152/>.

Tianqi Chen, Thierry Moreau, Ziheng Jiang, Lianmin Zheng, Eddie Yan, Meghan Cowan, Haichen Shen, Leyuan Wang, Yuwei Hu, Luis Ceze, Carlos Guestrin, and Arvind Krishnamurthy. TVM: an automated end-to-end optimizing compiler for deep learning. In *Proceedings of the 13th USENIX conference on Operating Systems Design and Implementation*, OSDI’18, pages 579–594, USA, October 2018a. USENIX Association. ISBN 978-1-931971-47-8.

Tianqi Chen, Lianmin Zheng, Eddie Yan, Ziheng Jiang, Thierry Moreau, Luis Ceze, Carlos Guestrin, and Arvind Krishnamurthy. Learning to optimize tensor programs. In *Proceedings of the 32nd International Conference on Neural Information Processing Systems*, NIPS’18, pages 3393–3404, Red Hook, NY, USA, December 2018b. Curran Associates Inc. doi:10.5555/3327144.3327258. URL <https://dl.acm.org/doi/10.5555/3327144.3327258>.

Kasia Świrydowicz, Noel Chalmers, Ali Karakus, and Tim Warburton. Acceleration of tensor-product operations for high-order finite element methods. *The International Journal of High Performance Computing Applications*, 33(4):735–757, July 2019. ISSN 1094-3420, 1741-2846. doi:10.1177/1094342018816368. URL <https://journals.sagepub.com/doi/10.1177/1094342018816368>.

Tianqi Chen and Carlos Guestrin. XGBoost: A Scalable Tree Boosting System. In *Proceedings of the 22nd ACM SIGKDD International Conference on Knowledge Discovery and Data Mining*, pages 785–794, San Francisco California USA, August 2016. ACM. ISBN 978-1-4503-4232-2. doi:10.1145/2939672.2939785. URL <https://dl.acm.org/doi/10.1145/2939672.2939785>.

Yuta Kawai and Hirofumi Tomita. Numerical Accuracy Necessary for Large-Eddy Simulation of Planetary Boundary Layer Turbulence Using the Discontinuous Galerkin Method. *Monthly Weather Review*, 151(6):1479–1508, June 2023. ISSN 0027-0644, 1520-0493. doi:10.1175/MWR-D-22-0245.1. URL <https://journals.ametsoc.org/view/journals/mwre/151/6/MWR-D-22-0245.1.xml>.

Yuta Kawai and Hirofumi Tomita. Development of a high-order global dynamical core using the discontinuous Galerkin method for an atmospheric large-eddy simulation (LES) and proposal of test cases: SCALE-DG v0.8.0. *Geoscientific Model Development*, 18(3):725–762, February 2025. ISSN 1991-9603. doi:10.5194/gmd-18-725-2025. URL <https://gmd.copernicus.org/articles/18/725/2025/>.

Xuanzhengbo Ren, Yuta Kawai, Hirofumi Tomita, Seiya Nishizawa, Takahiro Katagiri, Masatoshi Kawai, Tetsuya Hoshino, and Toru Nagai. Implementing Fast Modal Filtering of SCALE-DG. In *2024 IEEE International Conference on Cluster Computing Workshops (CLUSTER Workshops)*, pages 150–151, Kobe, Japan, September 2024. IEEE. ISBN 979-8-3503-8345-4. doi:10.1109/CLUSTERWorkshops61563.2024.00033. URL <https://ieeexplore.ieee.org/document/10740898/>.

Tejas S. Karkhanis and James E. Smith. Automated design of application specific superscalar processors: an analytical approach. In *Proceedings of the 34th annual international symposium on Computer architecture*, pages 402–411, San Diego California USA, June 2007. ACM. ISBN 978-1-59593-706-3. doi:10.1145/1250662.1250712. URL <https://dl.acm.org/doi/10.1145/1250662.1250712>.

RRZE-HPC/OSACA, October 2025. URL <https://github.com/RRZE-HPC/OSACA>. original-date: 2017-03-02T13:07:31Z.

Pierre Michaud, André Seznec, and Stéphan Jourdan. An Exploration of Instruction Fetch Requirement in Out-of-Order Superscalar Processors. *International Journal of Parallel Programming*, 29(1):35–58, February 2001. ISSN 0885-7458, 1573-7640. doi:10.1023/A:1026431920605. URL <https://link.springer.com/10.1023/A:1026431920605>.

A64FX Microarchitecture Manual v1.8.1, a. URL <https://github.com/fujitsu/A64FX/tree/master/doc>.

Andreas Abel and Jan Reineke. uops.info: Characterizing Latency, Throughput, and Port Usage of Instructions on Intel Microarchitectures. In *Proceedings of the Twenty-Fourth International Conference on Architectural Support for Programming Languages and Operating Systems*, pages 673–686, Providence RI USA, April 2019. ACM. ISBN 978-1-4503-6240-5. doi:10.1145/3297858.3304062. URL <https://dl.acm.org/doi/10.1145/3297858.3304062>.

Derek B. Noonburg and John P. Shen. Theoretical modeling of superscalar processor performance. In *Proceedings of the 27th annual international symposium on Microarchitecture - MICRO 27*, pages 52–62, San Jose, California, United States, 1994. ACM Press. ISBN 978-0-89791-707-0. doi:10.1145/192724.192730. URL <http://portal.acm.org/citation.cfm?doid=192724.192730>.

Sajid Ali, Tamer Abuhmed, Shaker El-Sappagh, Khan Muhammad, Jose M. Alonso-Moral, Roberto Confalonieri, Riccardo Guidotti, Javier Del Ser, Natalia Díaz-Rodríguez, and Francisco Herrera. Explainable Artificial Intelligence (XAI): What we know and what is left to attain Trustworthy Artificial Intelligence. *Information Fusion*, 99:101805, November 2023. ISSN 15662535. doi:10.1016/j.inffus.2023.101805. URL <https://linkinghub.elsevier.com/retrieve/pii/S1566253523001148>.

Scott M. Lundberg and Su-In Lee. A unified approach to interpreting model predictions. In *Proceedings of the 31st International Conference on Neural Information Processing Systems*, NIPS’17, pages 4768–4777, Red Hook, NY, USA, December 2017. Curran Associates Inc. ISBN 978-1-5108-6096-4. doi:10.5555/3295222.3295230. URL <https://dl.acm.org/doi/10.5555/3295222.3295230>.

Heike Jagode, Anthony Danalis, Giuseppe Congiu, Daniel Barry, Anthony Castaldo, and Jack Dongarra. Advancements of PAPI for the exascale generation. *The International Journal of High Performance Computing Applications*, 39(2):251–268, March 2025. ISSN 1094-3420, 1741-2846. doi:10.1177/10943420241303884. URL <https://journals.sagepub.com/doi/10.1177/10943420241303884>.

llvm-mca - LLVM Machine Code Analyzer — LLVM 22.0.0git documentation, b. URL <https://llvm.org/docs/CommandGuide/llvm-mca.html>.

Aleksandar Ilic, Frederico Pratas, and Leonel Sousa. Cache-aware Roofline model: Upgrading the loft. *IEEE Computer Architecture Letters*, 13(1):21–24, January 2014. ISSN 1556-6056. doi:10.1109/L-CA.2013.6. URL <http://ieeexplore.ieee.org/document/6506838/>.

Victoria Caparros Cabezas and Markus Puschel. Extending the roofline model: Bottleneck analysis with microarchitectural constraints. In *2014 IEEE International Symposium on Workload Characterization (IISWC)*, pages 222–231, Raleigh, NC, USA, October 2014. IEEE. ISBN 978-1-4799-6454-3 978-1-4799-6452-9. doi:10.1109/IISWC.2014.6983061. URL <http://ieeexplore.ieee.org/document/6983061/>.

Jan Laukemann, Julian Hammer, Johannes Hofmann, Georg Hager, and Gerhard Wellein. Automated Instruction Stream Throughput Prediction for Intel and AMD Microarchitectures. In *2018 IEEE/ACM Performance Modeling, Benchmarking and Simulation of High Performance Computer Systems (PMBS)*, pages 121–131, Dallas, TX, USA, November 2018. IEEE. ISBN 978-1-7281-0182-8. doi:10.1109/PMBS.2018.8641578. URL <https://ieeexplore.ieee.org/document/8641578/>.

Jan Laukemann, Julian Hammer, Georg Hager, and Gerhard Wellein. Automatic Throughput and Critical Path Analysis of x86 and ARM Assembly Kernels. In *2019 IEEE/ACM Performance Modeling, Benchmarking and Simulation of High Performance Computer Systems (PMBS)*, pages 1–6, Denver, CO, USA, November 2019. IEEE. ISBN 978-1-7281-5977-5. doi:10.1109/PMBS49563.2019.00006. URL <https://ieeexplore.ieee.org/document/9059263/>.

Andreas Abel, Shrey Sharma, and Jan Reineke. Facile: Fast, Accurate, and Interpretable Basic-Block Throughput Prediction. In *2023 IEEE International Symposium on Workload Characterization (IISWC)*, pages 87–99, Ghent, Belgium, October 2023. IEEE. ISBN 979-8-3503-0317-9. doi:10.1109/IISWC59245.2023.00023. URL <https://ieeexplore.ieee.org/document/10289219/>.

Matthew Leinhauser, René Widera, Sergei Bastrakov, Alexander Debus, Michael Bussmann, and Sunita Chandrasekaran. Metrics and Design of an Instruction Roofline Model for AMD GPUs, 2021. URL <https://arxiv.org/abs/2110.08221>. Version Number: 2.

Nan Ding, Muaaz Awan, and Samuel Williams. Instruction Roofline: An insightful visual performance model for GPUs. *Concurrency and Computation: Practice and Experience*, 34(20):e6591, September 2022. ISSN 1532-0626, 1532-0634. doi:10.1002/cpe.6591. URL <https://onlinelibrary.wiley.com/doi/10.1002/cpe.6591>.

Ruimin Shi, Gabin Schieffer, Maya Gokhale, Pei-Hung Lin, Hiren Patel, and Ivy Peng. ARM SVE Unleashed: Performance and Insights Across HPC Applications on Nvidia Grace. In Wolfgang E. Nagel, Diana Goehringer, and Pedro C. Diniz, editors, *Euro-Par 2025: Parallel Processing*, volume 15901, pages 33–47. Springer Nature Switzerland, Cham, 2026. ISBN 978-3-031-99856-0 978-3-031-99857-7. doi:10.1007/978-3-031-99857-7_3. URL https://link.springer.com/10.1007/978-3-031-99857-7_3. Series Title: Lecture Notes in Computer Science.

Dominic Kempf, René Heß, Steffen Müthing, and Peter Bastian. Automatic Code Generation for High-performance Discontinuous Galerkin Methods on Modern Architectures. *ACM Transactions on Mathematical Software*, 47(1):

1–31, March 2021. ISSN 0098-3500, 1557-7295. doi:10.1145/3424144. URL <https://dl.acm.org/doi/10.1145/3424144>.

Sam Kaufman, Phitchaya Phothilimthana, Yanqi Zhou, Charith Mendis, Sudip Roy, Amit Sabne, and Mike Burrows. A Learned Performance Model for Tensor Processing Units. *Proceedings of Machine Learning and Systems*, 3: 387–400, March 2021.

Yi Zhai, Yu Zhang, Shuo Liu, Xiaomeng Chu, Jie Peng, Jianmin Ji, and Yanyong Zhang. TLP: A Deep Learning-Based Cost Model for Tensor Program Tuning. In *Proceedings of the 28th ACM International Conference on Architectural Support for Programming Languages and Operating Systems, Volume 2*, pages 833–845, Vancouver BC Canada, January 2023. ACM. ISBN 978-1-4503-9916-6. doi:10.1145/3575693.3575737. URL <https://dl.acm.org/doi/10.1145/3575693.3575737>.

Chamika Sudusinghe, Gerasimos Gerogiannis, Damitha Lenadora, Charles Block, Josep Torrellas, and Charith Mendis. COGNATE: Acceleration of Sparse Tensor Programs on Emerging Hardware using Transfer Learning, 2025. URL <https://arxiv.org/abs/2506.00424>. Version Number: 2.

Christie Alappat, Nils Meyer, Jan Laukemann, Thomas Gruber, Georg Hager, Gerhard Wellein, and Tilo Wettig. Execution-Cache-Memory modeling and performance tuning of sparse matrix-vector multiplication and Lattice quantum chromodynamics on A64FX. *Concurrency and Computation: Practice and Experience*, 34(20):e6512, September 2022. ISSN 1532-0626, 1532-0634. doi:10.1002/cpe.6512. URL <https://onlinelibrary.wiley.com/doi/10.1002/cpe.6512>.

RRZE-HPC/ECM-Model: Knowledge base how to setup the ECM model inputs, c. URL <https://github.com/RRZE-HPC/ECM-Model>.